

Resonant absorption and radiation in transmon qubits

by

Owen M. Rafferty

A thesis submitted in partial fulfillment of
the requirements for the degree of

Bachelor of Science with Honors in the Major
(Physics)

at the

UNIVERSITY OF WISCONSIN–MADISON

May 2021

Supervisor:

Professor Robert McDermott

Abstract

Superconducting qubits are resonant absorbers of pair-breaking radiation. The metal pads that form the qubit capacitance support standing wave modes at frequencies of order 100 GHz; these modes are strongly coupled to free-space impedance through their electric dipole moment. While the antenna mode of the 3D transmon qubit is easily seen to be a resonant dipole, other 2D qubit types can be understood as the aperture duals of wire loop antennas or folded dipoles. For typical Josephson junction parameters, the junction provides a reasonable conjugate match to the fundamental antenna mode. We calculate the contribution to quasiparticle poisoning from resonant absorption of blackbody radiation. We extend our analysis to dissipation at the qubit frequency, where radiative losses provide an ultimate limit to qubit energy relaxation time. A clear understanding of the spurious antenna modes of qubits will allow designs that are insensitive to pair-breaking radiation and that display reduced radiative losses at the qubit frequency. Moreover, this physics could be exploited to realize a new class of high-performance detectors for precision spectroscopy of the cosmic microwave background or of photons transduced from dark matter axions.

Acknowledgments

I must, first and foremost, thank my advisor, Professor Robert McDermott. I first approached Robert after developing a vague interest in quantum information while taking his quantum mechanics course, but, once in the lab, struggled to get attached to a project for quite some time. Nonetheless, Robert frequently encouraged me, and I eventually began working on what is detailed in this thesis. He has taught me an inordinate volume of information over the past year, continuously pushed me to progress this project, and has been a great source of optimism for my future.

I could not have made it through college and into graduate school without the support and encouragement of my family, particularly my parents Hugh and Tina, sister Madeline and brother-in-law Dan, grandparents Bino and Karen, and cousin Christopher, as well as that of various physics classmates, roommates, and friends over the years—especially Abby, Josh, Jacqui, Yichen, Michael, Brett, Ethan, Gia, Hunter, Sam, and Seamus.

This work was supported by the Hilldale Undergraduate Research Fellowship, and by the Fermi National Accelerator Laboratory, managed and operated by Fermi Research Alliance, LLC under Contract No. DE-AC02-07CH11359 with the U.S. Department of Energy.

Contents

Abstract i

Contents iii

List of Figures iv

1 Introduction 1

2 Spurious Antenna Modes 4

2.1 *Babinet's Principle: Wire/Aperture Duality* 4

2.2 *Resonant Antenna Modes of Typical Transmon Structures* 7

2.3 *Coupling Efficiency to the Josephson Junction* 11

2.4 *Implications for Quasiparticle Poisoning* 16

2.5 *Dissipation at the Qubit Frequency* 17

3 Conclusion, Experiments, and Applications 20

3.1 *Outlook* 20

3.2 *Experiments* 21

3.3 *Applications* 24

Colophon 27

Bibliography 28

List of Figures

2.1	Wire/aperture duality	6
2.2	Typical 2D qubit structures and their wire antenna duals	8
2.3	Antenna impedance of single-ended transmons	10
2.4	Resonant antenna mode of the Xmon qubit	12
2.5	Resonant antenna mode of the differential transmon	14
2.6	Resonant dipole antenna mode of the 3D transmon	15
3.1	Upward QP-induced transitions vs Temperature	22
3.2	Weakly charge-sensitive transmons of various scales	23
3.3	Device scale-dependent impedance simulations	24
3.4	Folded monopole antenna array	26

Chapter 1

Introduction

This chapter is a reformatted and expanded version of Section I of Ref. [1].

Superconducting qubits are implemented as low-loss, nonlinear [2] microwave modes [3]. The mode frequency is typically in the range 3-10 GHz; electromagnetic coupling of the qubit to the environment is carefully controlled in order to minimize decoherence. Environmental fluctuations at the qubit frequency induce relaxation, while low-frequency fluctuations induce qubit dephasing. Progress in understanding the electromagnetic environment of the qubit has resulted in steady improvements in qubit fidelity over the last two decades.

Qubit devices are typically cooled to temperatures below 20 mK in order to suppress dissipation from quasiparticle excitations out of the superconducting ground state. At these temperatures, the equilibrium density of quasiparticles should be exponentially small. Nevertheless, researchers find quasiparticle density of order $1 \mu\text{m}^{-3}$ [4–7], tens of orders of magnitude larger than the thermal equilibrium quasiparticle density expected from theory. Nonequilibrium quasiparticles tunnel across the Josephson junctions, inducing both excitation and relaxation [8]. Recent works have shown that gamma rays and cosmic rays can be a source of nonequilibrium quasiparticles [9, 10]; while particle impacts give rise to damaging correlated errors due to phonon-mediated quasiparticle poisoning [11],

the event rate is too low and the escape rate of athermal phonons from the chip too high to account for the background population of quasiparticles. Other studies point to pair-breaking radiation as a potentially significant source of quasiparticle generation [6, 12], and researchers have demonstrated improvements by shielding devices from blackbody radiation and by introducing in-line filters to block pair-breaking photons from higher temperature stages [13, 14]. The model in [12] predicts narrowband absorption of photons with an energy greater than the superconducting gap energy, $\hbar\omega > 2\Delta$, as well as a ratio of upward to downward qubit transitions induced by this photon-assisted mechanism near unity. However, the mechanism by which photons couple to the qubit junction has not been understood.

In this thesis, we show that transmon qubit structures [15, 16] act as resonant absorbers of pair-breaking radiation at frequencies far outside the qubit operating range, in the 10s of GHz to THz. While environmental fluctuations at these frequencies have no direct effect on qubit operation, they can break Cooper pairs, giving rise to quasiparticle poisoning that can degrade qubit coherence. The spurious antenna modes intrinsic to the qubit structure provide a perversely efficient route to channel quasiparticles to the qubit junction, where they do the most damage. We calculate the contribution to quasiparticle poisoning from the resonant absorption of blackbody radiation. In addition, our analysis provides a straightforward means to calculate the limit to qubit energy relaxation time imposed by radiation at the qubit frequency. We find that state-of-the-art qubit devices are approaching the limit to qubit T_1 imposed by radiative loss.

This thesis is organized as follows. In Section 2.1, we review the basics of antenna physics and describe Babinet's principle [17], which allows us to map conventional 2D qubit geometries to dual wire antenna structures. In Section 2.2, we describe the fundamental resonant modes of specific qubit geometries that are pursued for quantum computing: the single-ended transmon with circular and rectangular island; the Xmon [18]; the differential transmon [19, 20]; and the 3D transmon [21]. In Section 2.3, we consider the coupling of

energy from the resonant antenna mode to the Josephson junction, and we show that for typical parameters the junction presents a reasonable conjugate match to the radiation impedance of the antenna. In addition, we present detailed calculations of coupling efficiency and antenna noise bandwidth for specific qubit geometries. In Section 2.4, we present a simple analysis that allows us to quantify the contribution to quasiparticle generation at the junction from resonant absorption of broadband blackbody radiation. In Section 2.5, we quantify the contribution to qubit dissipation from radiation at the qubit frequency, for which the qubit structure can be modeled as an electrically small antenna. Finally, in Chapter 3 we conclude with a brief discussion of implications of this analysis for other qubit types, of ongoing experiments attempting to test the model described here, and of prospects for exploiting antenna coupling to pair-breaking photons to realize a new class of quantum sensors for dark matter detection and precision spectroscopy.

Chapter 2

Spurious Antenna Modes

In this chapter, we describe how typical transmon structures support standing-wave resonances and how power is coupled to their Josephson junction. This chapter is a reformatted version of Sections II–VI of Ref. [1].

2.1 Babinet’s Principle: Wire/Aperture Duality

Conducting structures that support time-varying currents and voltages will radiate efficiently at frequencies corresponding to standing wave resonances. The prototypical example is the half-wave dipole antenna; here, current is injected into a central feed point, which is a low-impedance current antinode. Current vanishes at the ends of the antenna arms; at the half-wave resonance, constructive interference leads to a standing wave. Radiation to the far field represents a real impedance, while energy stored in the near-field region represents an imaginary impedance. We will refer to this type of antenna, consisting of sparse conducting features that support time-varying currents that couple to the radiation field, as a *wire antenna*.

While the 3D transmon [21] is readily understood as a resonant half-wave dipole with fundamental resonance at a frequency of order 100 GHz, the dominant radiation mode of 2D planar qubits is not immediately obvious. The qubit is typically realized as a small

superconducting island embedded in a near-continuous superconducting groundplane and connected to ground via one or more Josephson junctions. Due to symmetry, the lowest nonvanishing moment of the island+groundplane will be an electric quadrupole, which is expected to present a rather small radiation resistance. To understand the radiation mode of 2D transmon qubits, we use Babinet’s principle [17], which allows us to map from 2D qubit geometries to their wire antenna dual structures. We find that 2D qubits can be seen as the *aperture antenna* duals of common wire antennas such as the folded half-wave dipole or the resonant loop antenna. With this insight, it is clear that 2D superconducting qubits, of the type currently explored for fault-tolerant arrays [22], noisy intermediate-scale quantum processors [23], or demonstrations of quantum supremacy [24], will radiate at a fundamental frequency where the wavelength is matched to the qubit perimeter.

According to Babinet’s principle, a wire antenna is dual to the aperture structure where conductor is replaced by empty space in an otherwise continuous conducting plane. If the wire antenna is fed by a current injected into a low-impedance current antinode, feed in the aperture dual is a voltage coupled to the high-impedance voltage antinode. The complex radiation impedances of the wire antenna Z_w and its aperture dual Z_a are related by the formula

$$Z_a Z_w = \frac{\eta^2}{4}, \quad (2.1)$$

where $\eta = \sqrt{\mu_0/\epsilon_0} \approx 377 \Omega$ is the impedance of free space. As an example, the capacitance C_a of a planar electrode embedded in a groundplane in aperture space is simply related to the inductance L_w of the complementary loop in wire space: $C_a = 4(\epsilon_0/\mu_0)L_w$ (see Fig. 2.1a).

Here we are concerned with transmon qubit structures fabricated using thin-film processing techniques on planar substrates. As an example of the dual mapping from wire antenna to aperture antenna, we consider in Fig. 2.1b a wire antenna implemented using rectangular thin-film electrodes with length l and width w , both assumed to be large compared to film thickness; this structure is the basis for the 3D transmon qubit [21], considered

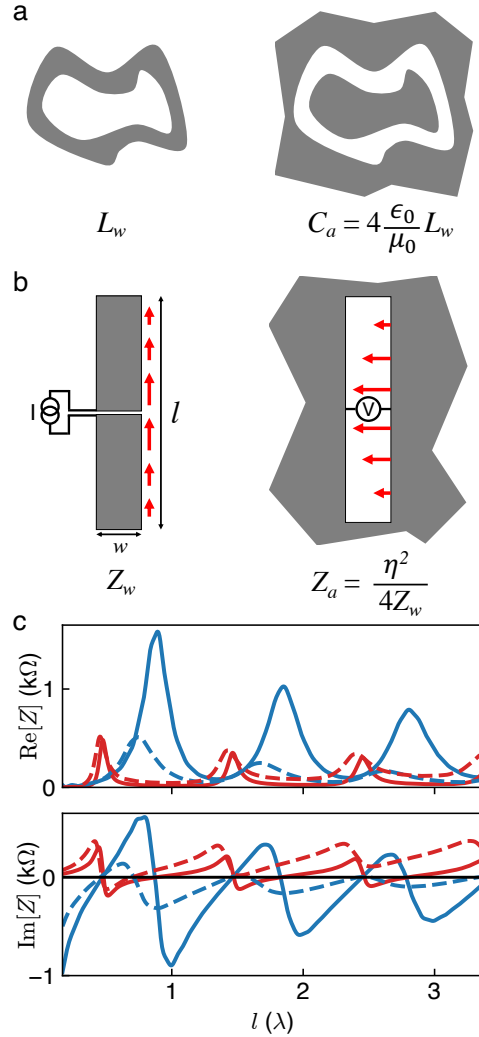


Figure 2.1: Wire/aperture duality. (a) The planar loop in wire space is dual to the planar capacitor embedded in a groundplane in aperture space. (b) Planar wire antenna and its aperture dual. The antennas have length l and width w , both large compared to film thickness. Here, the direction and magnitude of E -fields at the fundamental modes are shown schematically by red arrows. (c) Simulated real and imaginary parts of the antenna impedance Z of the wire (blue) and aperture (red) structures at aspect ratio $l/w \approx 200$ (solid) and $l/w \approx 20$ (dashed).

in detail below. The structure is dual to the aperture or slot antenna shown in the right panel of Fig. 2.1b. In mapping from the wire antenna to the aperture dual, a low-impedance point is mapped to high impedance and vice versa; in addition, the polarization of the radiated field is rotated by 90° . However the standing wave mode and the dipole radiation pattern are the same. In Fig. 2.1c, we plot the real and imaginary parts of the radiation impedance of these two antennas calculated¹ using a finite-element solver [26] for aspect ratio $l/w = 200$ and 20 . In the limit of large l/w , the wire antenna reduces to the ideal resonant half-wave dipole. For structures with lower aspect ratio, sharp resonant structure in Z is smoothed out, and resonances are shifted to lower frequency. Peaks in the radiation resistance of the wire antenna correspond to low radiation resistance for the aperture dual, and vice versa.

2.2 Resonant Antenna Modes of Typical Transmon Structures

In Fig. 2.2, we show simplified layouts of various 2D qubit geometries along with their wire duals. In the case of a circular transmon island, the structure is the dual of the conventional loop antenna, which involves a fundamental resonance when the loop circumference is matched to the wavelength. The transmon qubit with rectangular island is mapped to the resonant half-wave folded dipole antenna. Here, for the aperture (wire) structure, there are voltage (current) nodes at the ends of the antenna arms, so that E -fields interfere constructively across the arms of the structure. The Xmon structure of [18] is mapped to a variant of the folded dipole antenna, involving a fundamental resonance where E -fields from the horizontal arms interfere constructively, while E -fields from the vertical arms

¹These simulations were executed using the finite-difference time-domain method. Conducting elements were modeled as perfect electrical conductors so as to eliminate ohmic losses—we do not find the distinction between a superconductor and a perfect conductor [25] to be relevant here. In wire antenna simulations, gap width was taken to be order $1/100$ times the length of the resonant wavelength, and in aperture antenna simulations, ground plane linear dimension was taken to be order 10 times the scale of the device.

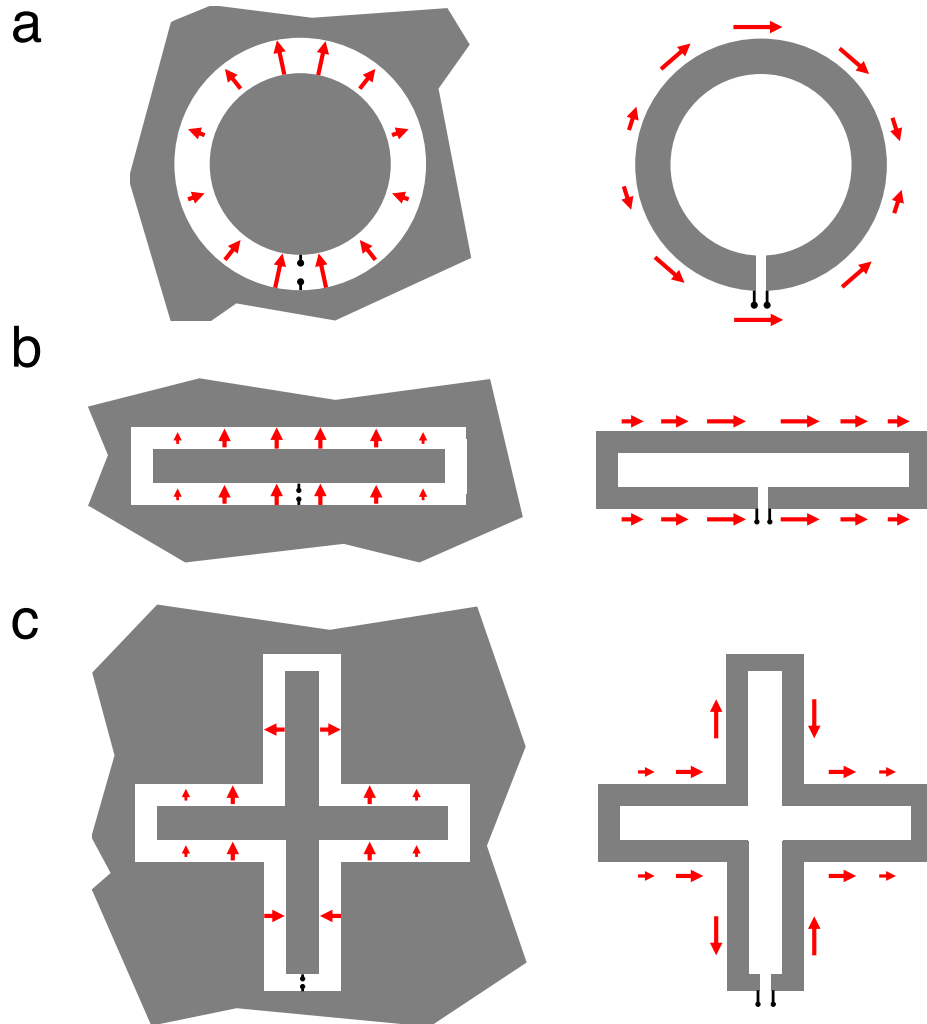


Figure 2.2: Typical 2D qubit structures and their wire antenna duals. (a) The transmon with circular island is dual to the resonant loop antenna. (b) The transmon with rectangular island is dual to the folded half-wave dipole antenna. (c) The Xmon qubit [18] supports a resonant antenna mode corresponding to device perimeter equal to one full wavelength. For the structure shown here, the horizontal arms radiate like a folded dipole, while the vertical arms do not couple to the far field. In this figure, the direction and magnitude of E -fields at the fundamental modes are shown schematically by red arrows.

interfere destructively.

In Fig. 2.3, we plot the real and imaginary parts of the antenna impedance for the circular and rectangular transmon geometries, for various device aspect ratios. The fundamental full-wave resonance corresponds to a peak in the real part of the antenna impedance. In the vicinity of this resonance, the antenna presents an inductive impedance with positive imaginary part. As we will show below, such a structure allows an excellent conjugate match to the impedance of a Josephson junction, providing an efficient means to couple pair-breaking radiation directly to the junction.

We note that the wire/aperture duality extends to the dielectric or magnetic medium in which the antenna is embedded: relative permittivity in one space is mapped to relative permeability in the complementary dual space. That is, for relative permittivity and permeability ϵ_r, μ_r in the aperture antenna space and relative permittivity and permeability ϵ'_r, μ'_r in the dual wire antenna space, we have $\epsilon'_r = \mu_r, \mu'_r = \epsilon_r$. Here we are concerned with aperture antenna structures fabricated on dielectric substrates with relative permittivity ϵ_r . In the limit of an infinitely thick substrate, this is equivalent to the same antenna structure embedded in a uniform dielectric medium with effective permittivity $\epsilon_{\text{eff}} = (1 + \epsilon_r) / 2$. This structure is then mapped to a wire antenna embedded in a magnetic medium with permeability $\mu'_r = \epsilon_{\text{eff}}$. In the following analysis of specific 2D qubit geometries, we consider an infinitely thick substrate with relative permittivity $\epsilon_r = 11$, a reasonable match to either silicon ($\epsilon_r = 11.7$) or sapphire (anisotropic; $\epsilon_r = 8.9-11.1$). For dielectric substrates of finite thickness, standing waves in the substrate can give rise to additional resonant structure in the radiation impedance of the antenna. In general, accurate modeling will require full numerical simulation that takes into account the substrate dimensions, including placement of the qubit structure on the substrate chip.

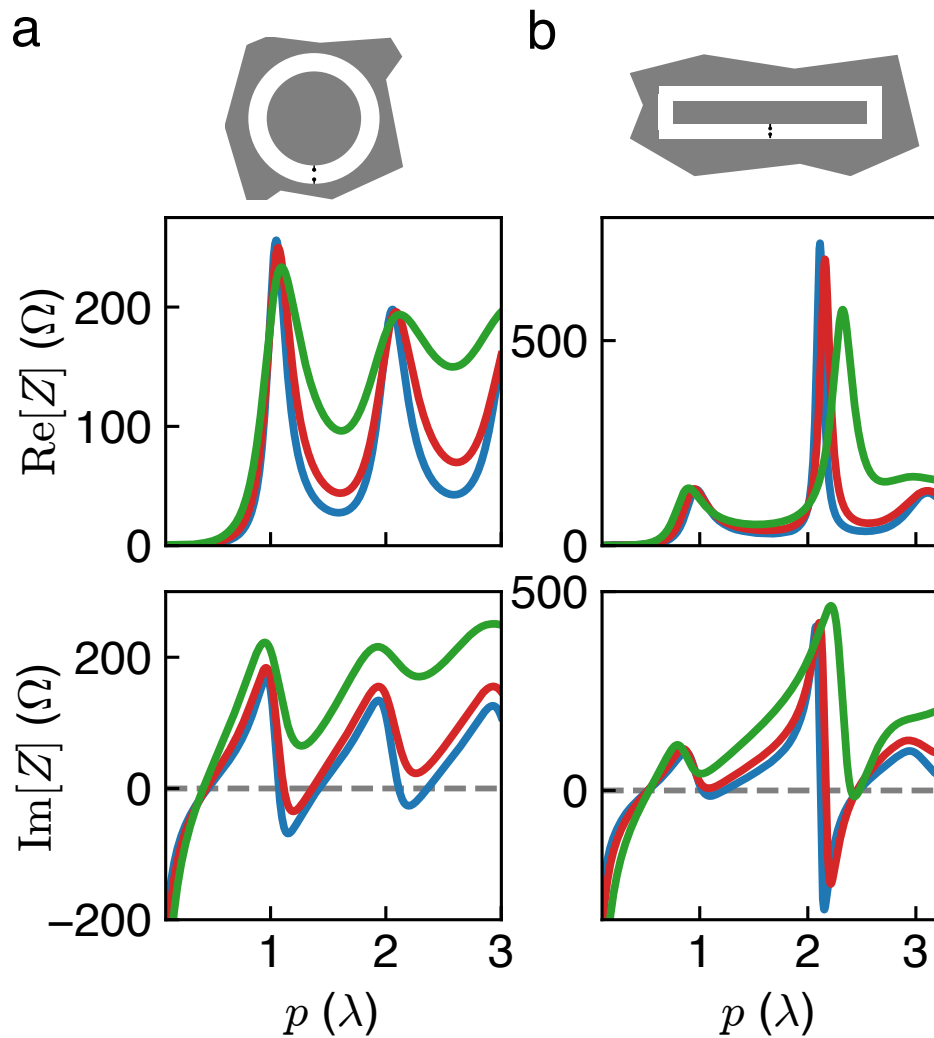


Figure 2.3: Antenna impedance of single-ended transmons. (a) Real and imaginary parts of the antenna impedance of circular transmons with aspect ratios $p/w = 100$ (blue), 50 (red), and 20 (green), where p is the perimeter at the center of the gap and w is the width of the gap. (b) Real and imaginary parts of the antenna impedance of rectangular transmons with aspect ratios and trace colors as in (a).

2.3 Coupling Efficiency to the Josephson Junction

We are concerned with absorption of radiation at a frequency above the superconducting gap; in this case, we can model the junction as a resistance equal to the tunnel resistance R_n (of order 5-10 k Ω) shunted by the junction self-capacitance C_j (typically 1-10 fF). The tunnel resistance is related to the critical current I_0 via the Ambegaokar-Baratoff relation [27]:

$$R_n = \frac{\pi\Delta}{2eI_0}. \quad (2.2)$$

For aluminum, we have $2\Delta/e = 380 \mu\text{V}$ and $I_0R_n \approx 300 \mu\text{V}$. We can map the junction resistance and self capacitance to a complex impedance Z_j consisting of a (frequency-dependent) real resistance in series with a negative imaginary impedance:

$$Z_j = \frac{1 - j\omega\tau}{1 + \omega^2\tau^2}R_n, \quad (2.3)$$

where $\tau \equiv R_nC_j$. As a result, the junction presents a capacitive load to the antenna, with radiation impedance Z_{rad} . Optimal power transfer is achieved when the conjugate matching condition is satisfied: $Z_{\text{rad}} = Z_j^*$. In the case of mismatch between the junction and the antenna, the power transferred to the junction is reduced compared to the maximum available power. We define coupling efficiency e_c as follows:

$$e_c = 1 - |\Gamma|^2, \quad (2.4)$$

where

$$\Gamma = \frac{Z_{\text{rad}} - Z_j^*}{Z_{\text{rad}} + Z_j}. \quad (2.5)$$

We define an antenna noise bandwidth Δf_N by integrating e_c over frequency:

$$\Delta f_N = \int e_c df. \quad (2.6)$$

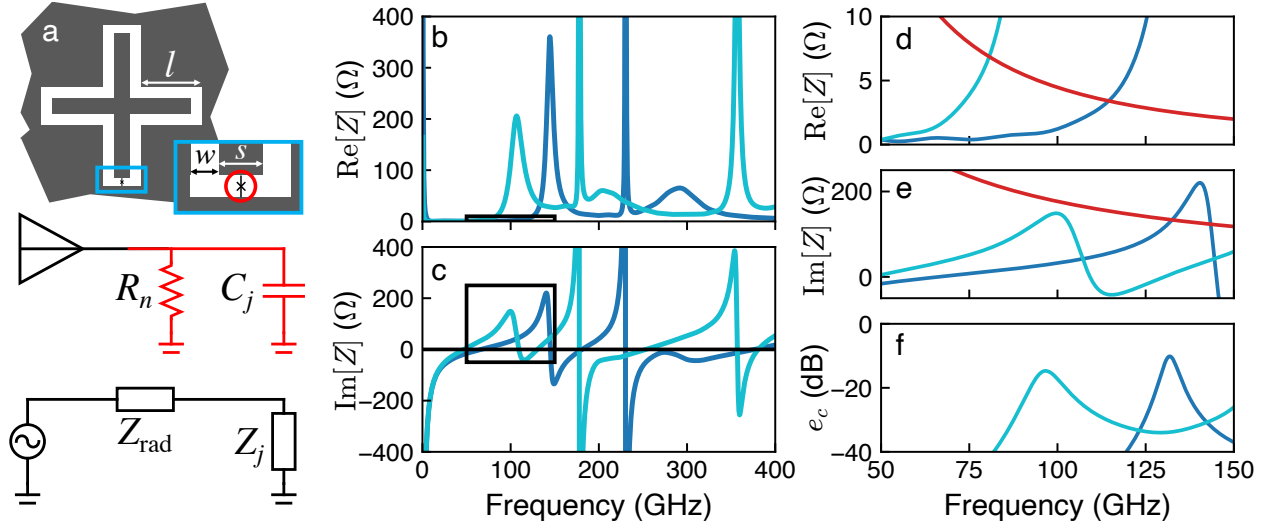


Figure 2.4: Resonant antenna mode of the Xmon qubit. (a) Geometry of the Xmon qubits described in [18]. The center trace width is s ; gap to the groundplane is w ; and length of a single arm is l . The junction is modeled as a real tunnel resistance R_n in parallel with the junction self-capacitance C_j . Real (b) and imaginary (c) parts of Xmon antenna impedance for devices with $l = 130 \mu\text{m}$, $s = 8 \mu\text{m}$, and $w = 4 \mu\text{m}$ (blue) and $l = 165 \mu\text{m}$, $s = 24 \mu\text{m}$, and $w = 24 \mu\text{m}$ (cyan). Real (d) and imaginary (e) parts of Z_{rad} and Z_j^* (red) in the vicinity of the fundamental antenna resonance. Here we take $R_n = 7 \text{ k}\Omega$ and $C_j = 9 \text{ fF}$. (f) Frequency-dependent coupling efficiency e_c for the two Xmon devices. For the larger device, the coupling efficiency peaks at 97 GHz with antenna noise bandwidth $\Delta f_N = 1.8 \text{ GHz}$. For the smaller device, coupling efficiency peaks at 130 GHz with noise bandwidth $\Delta f_N = 2.5 \text{ GHz}$.

As we will see in Section 2.4 below, this noise bandwidth determines the integrated power of pair-breaking radiation coupled to the junction.

Xmon Qubit

In Fig. 2.4 we plot Z_{rad} and Z_j^* for two of the Xmon qubit devices described in [18]. The device dimensions are taken from the manuscript; the (compound) junction tunnel resistance $R_n = 7 \text{ k}\Omega$ is inferred from the reported mode frequency and anharmonicity, and the junction capacitance $C_j = 9 \text{ fF}$ is taken from the reported area of the junctions, using a specific capacitance of $75 \text{ fF}/\mu\text{m}^2$. We assume a semi-infinite substrate with relative permittivity $\epsilon_r = 11$, corresponding to $\epsilon_{\text{eff}} = 6$. For the device with narrow traces and narrow gap, we find reasonable power match to the junction at a frequency of 130 GHz

and a noise bandwidth $\Delta f_N = 1.8$ GHz. For the device with wider trace width and wider gap, the resonance is pulled downward to around 97 GHz and we find $\Delta f_N = 2.5$ GHz.

Differential Qubits

A number of groups use differential qubits, where the qubit capacitance is formed from two superconducting islands with no galvanic connection to the circuit groundplane [19]. It has been argued that this symmetric construction provides additional protection against environmental fluctuations [28]. The resonant radiation mode of these structures can be understood simply from the wire antenna dual. In Fig. 2.5a, we show schematic diagrams of a differential qubit along with its wire dual. The wire dual can be viewed as a “doubled” folded half-wave dipole antenna, with a single feed branch and two parallel return branches. The radiation pattern and radiation resistance are expected to be identical to those for the conventional folded dipole. We have calculated the radiation resistance Z_{rad} for the differential qubit shown in Fig. 2.5a, which is a slight simplification of the qubit geometry described in [20]; results are shown in Fig. 2.5b, along with Z_j^* corresponding to a junction with $R_n = 7$ k Ω and $C_j = 9$ fF. The folded dipole resonance of the structure occurs at 110 GHz, and the device presents an excellent conjugate match to the junction. In Fig. 2.5c, we plot the antenna coupling efficiency for this qubit in the vicinity of the fundamental resonance. We find an antenna noise bandwidth $\Delta f_N = 2.8$ GHz, comparable to the single-ended Xmon qubit.

At low frequencies, these structures are dual to electrically small magnetic quadrupoles. Symmetry-based suppression of the dipole moment will provide protection against dissipation from radiation. This case is discussed in more detail in Section 2.5 below.

3D Transmon

The dominant radiation mode of the 3D transmon is that of a resonant half-wave dipole. In Fig. 2.6a we reproduce the geometry of the qubit described in [21], and in Fig. 2.6b

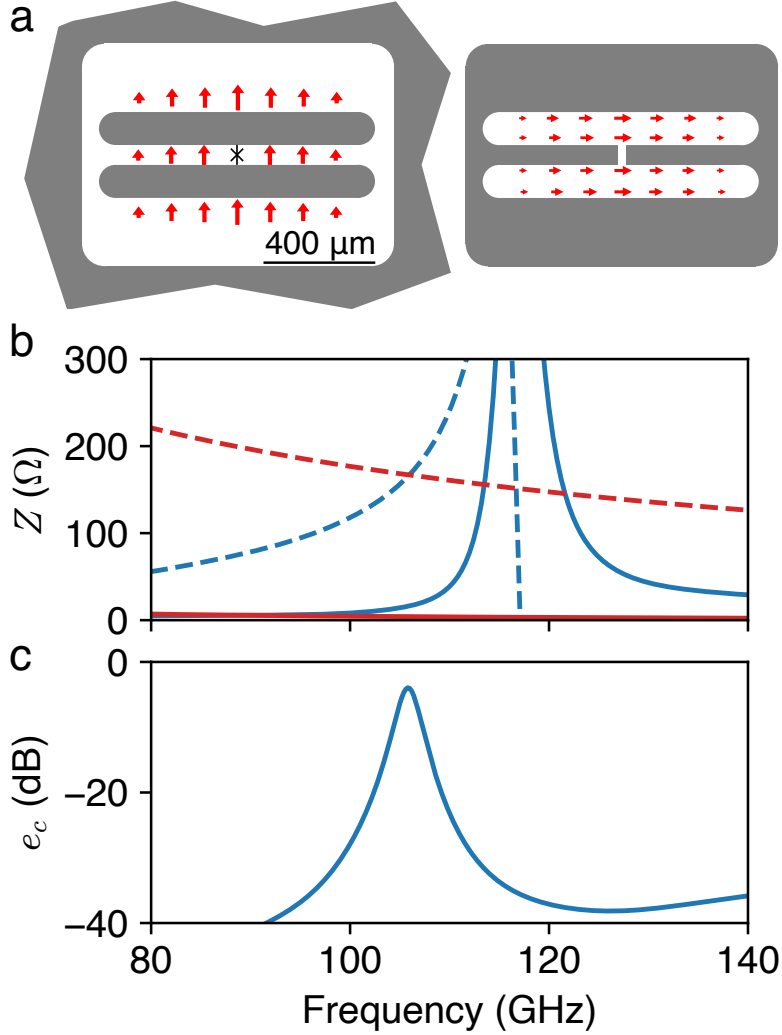


Figure 2.5: Resonant antenna mode of the differential transmon. (a) Simplified layout of the differential transmon and its wire antenna dual. The fundamental resonance corresponds to round trip around one island equal to a full wavelength. Here the direction and magnitude of E -fields at the fundamental resonance are shown schematically by red arrows. (b) Real (solid blue) and imaginary (dashed blue) parts of antenna impedance Z_{rad} of the differential qubit structure of [20], along with real (solid red) and imaginary (dashed red) parts of the conjugate junction impedance Z_j^* for $R_n = 7 \text{ k}\Omega$ and $C_j = 9 \text{ fF}$. (c) Frequency-dependent coupling efficiency e_c calculated from (b).

we plot Z_{rad} and Z_j^* for $R_n = 7 \text{ k}\Omega$, $C_j = 9 \text{ fF}$. Here we have taken $\epsilon_{\text{eff}} = 6$, which would correspond to an infinitely thick substrate with $\epsilon_r = 11$. Given the large dimensions of the qubit capacitor pads, this is clearly an oversimplification; more detailed modeling would be required for an accurate extraction of ϵ_{eff} . Within our simplified model, we find a

reasonable conjugate match to the junction at a frequency of 150 GHz, with antenna noise bandwidth $\Delta f_N = 4.4$ GHz.

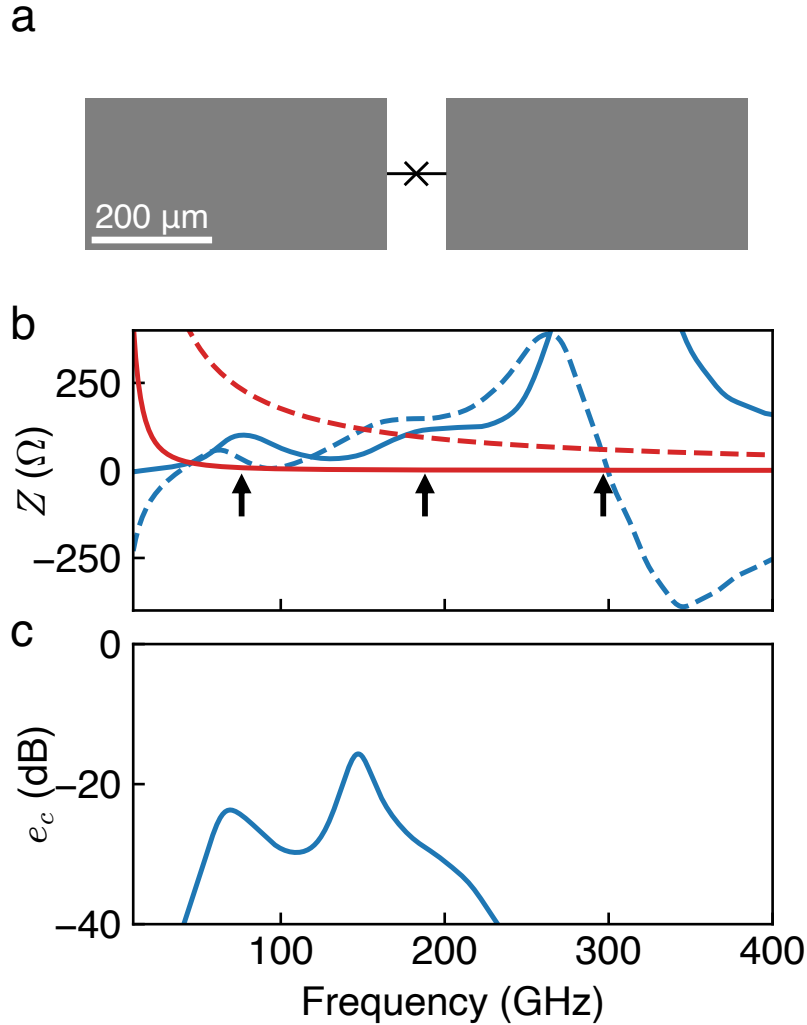


Figure 2.6: Resonant dipole antenna mode of the 3D transmon. (a) Device geometry (from [21]). (b) Real (solid blue) and imaginary (dashed blue) parts of antenna impedance Z_{rad} of the 3D qubit, along with real (solid red) and imaginary (dashed red) parts of the conjugate junction impedance Z_j^* for $R_n = 7$ kΩ and $C_j = 9$ fF. Arrows indicate the $\lambda/2$, $3\lambda/2$, and $5\lambda/2$ dipole resonance frequencies calculated from the dimensions of the structure. (c) Frequency-dependent coupling efficiency e_c calculated from (b).

2.4 Implications for Quasiparticle Poisoning

Thus, typical transmon structures act as highly efficient resonant absorbers of pair-breaking radiation. The coupling of pair-breaking photons to the spurious antenna mode is particularly damaging for the qubit, as the generated quasiparticles are created directly at the junction. The photon-assisted quasiparticle generation mechanism can induce both upward and downward qubit transitions [12]. Moreover, due to spatial inhomogeneities in the superconducting gap, the generated quasiparticles might remain localized near the junction, where they could tunnel back and forth repeatedly, giving rise to additional qubit transitions.

To connect the power spectral density of pair-breaking photons to a rate of quasiparticle generation at the qubit junction, we assume coupling of the qubit antenna to a single polarization and a single mode of the blackbody radiation field at temperature T . The blackbody power spectral density is given by

$$S(f, T) = \frac{hf}{e^{hf/k_B T} - 1}. \quad (2.7)$$

The total power coupled to the qubit junction is determined by integrating over the frequency-dependent coupling efficiency $e_c(f)$:

$$\begin{aligned} P &= \int S(f, T) e_c(f) df \\ &\approx \frac{hf_0}{e^{hf_0/k_B T} - 1} \Delta f_N, \end{aligned} \quad (2.8)$$

where f_0 is the frequency of maximum power transfer between the qubit antenna structure and the junction, and where Δf_N is defined in Eq. 2.6 above. The rate Γ_{pa} of photon-assisted quasiparticle poisoning events at the junction is therefore given by

$$\Gamma_{\text{pa}} = \frac{\Delta f_N}{e^{hf_0/k_B T} - 1}. \quad (2.9)$$

We take the larger Xmon qubit of Section 2.3 as an example. For $f_0 = 97$ GHz and $\Delta f_N = 1.8$ GHz, we find that a rate $\Gamma_{\text{pa}} = 300$ Hz of quasiparticle poisoning events (taken, e.g., from [29]) corresponds to an effective blackbody temperature $T = 300$ mK.

All transmon qubits analyzed here involve a resonant antenna mode at a frequency of order 100 GHz; this frequency is set by the overall scale of the device. As devices typically target a rather narrow range of qubit charging energy, it is understandable that the fundamental resonant antenna modes occupy a similarly small range of frequency. Moreover, typical junctions are reasonably well matched to the radiation impedance of the antenna mode, yielding noise bandwidth in the range 2-5 GHz. The consistency of antenna mode frequency and bandwidth across different qubit types leads us to conclude that coupling to blackbody radiation with effective temperature of order 300 mK is a likely explanation for the excess quasiparticles observed in superconducting qubit experiments.

2.5 Dissipation at the Qubit Frequency

The mapping of an aperture qubit to its wire antenna dual provides a particularly simple means to calculate the contribution to qubit dissipation from radiation. Qubit T_1 time is calculated from the real part of the admittance shunting the junction. If we neglect sources of loss other than radiation to the environment, we have

$$T_1 = \frac{C}{\text{Re}[Y_a(\omega_{01})]}, \quad (2.10)$$

where C is the qubit capacitance, Y_a is the radiation admittance of the aperture antenna formed by the qubit island and groundplane, and ω_{01} is the qubit transition frequency. From Babinet's principle, we have $Y_a = 4Z_w/\eta^2$, where Z_w is the radiation impedance of the wire antenna that is dual to the qubit structure. As a result, we have

$$T_1 = \frac{\eta^2}{4} \frac{C}{\text{Re}[Z_w(\omega_{01})]}. \quad (2.11)$$

Thus, knowledge of the radiation resistance of the wire antenna that is dual to the qubit structure allows straightforward calculation of the radiation limit to qubit T_1 .

We consider the simple case of a transmon with circular island embedded in a circular cavity in a continuous groundplane; we assume an effective permittivity ϵ_{eff} . The structure is the aperture dual of a wire loop antenna embedded in a magnetic medium with relative permeability $\mu'_r = \epsilon_{\text{eff}}$. We first take the limit of an infinitesimal wire width, for which radiation resistance can be calculated analytically:

$$\text{Re}[Z_w] = \frac{8}{3}\pi^5\epsilon_{\text{eff}}^{1/2}\eta\left(\frac{r}{\lambda}\right)^4. \quad (2.12)$$

We find a limit to qubit T_1 given by

$$T_1 = \frac{3}{2\pi}\epsilon_{\text{eff}}^{-5/2}\eta C\left(\frac{c}{\omega_{01}r}\right)^4, \quad (2.13)$$

where c is the speed of light in vacuum.

For a circular transmon island with radius r_i embedded in a circular cavity in the groundplane with finite gap width w , we calculate $\text{Re}[Z_w]$ numerically using the method outlined in [30]. For aspect ratio $w/r_i \lesssim 0.2$, the radiation resistance of the structure is well approximated by

$$\text{Re}[Z_w] = \frac{8}{3}\pi^5\epsilon_{\text{eff}}^{1/2}\eta\left(\frac{r_i}{\lambda}\right)^4\left(1 + 2.1\frac{w}{r_i}\right). \quad (2.14)$$

For typical qubit parameters, the correction to $\text{Re}[Z_w]$ due to finite gap width will be of order 10-30%.

For arbitrary qubit island geometry, we employ the same analysis, with the replacement $\pi r_i^2 \rightarrow A$, where A is the area of the qubit island.

Returning to Eq. 2.13, if we take $C = 100$ fF, $\omega_{01}/2\pi = 5$ GHz, and $r = 100$ μm , we find a radiative limit to qubit T_1 of 1.5 ms for $\epsilon_{\text{eff}} = 1$, and of 17 μs for $\epsilon_{\text{eff}} = 6$. The latter choice of ϵ_{eff} corresponds to an infinitely thick substrate with relative permittivity $\epsilon_r = 11$.

For a device fabricated on a substrate with thickness of order several hundred microns, considerably less than the wavelength at the qubit frequency, we expect that the effective permittivity will be suppressed from the value $\epsilon_{\text{eff}} = (\epsilon_r + 1)/2$. More detailed modeling of finite substrate effects will be needed to achieve a quantitative understanding of the radiative limit to qubit T_1 , which scales with effective permittivity as $\epsilon_{\text{eff}}^{-5/2}$.

In the case of the differential qubit [20], radiative losses are suppressed by symmetrization of the structure: the wire dual can be viewed as a magnetic quadrupole. For practical devices, however, the symmetry of the structure will be broken, and radiative losses will be dominated by the magnetic dipole moment associated with the area of unsymmetrized structures.

For the 3D transmon qubit, the radiation limit to T_1 is very severe for a device looking out at free space, as radiation from an electric dipole scales as $(r/\lambda)^2$. However, encapsulation of the qubit chip in a conducting cavity provides a Purcell suppression of the environmental density of states that protects the qubit from radiative loss [16].

Chapter 3

Conclusion, Experiments, and Applications

This chapter is a reformatted and expanded version of Section VII of Ref. [1].

3.1 Outlook

In conclusion, we have described the resonant coupling of superconducting qubit structures to pair-breaking photons via a spurious antenna mode. While the analysis presented here focuses on the transmon qubit, it can readily be extended to other qubit types, including fluxonium [31] and the capacitively shunted flux qubit [32]. The same considerations can be applied to microwave kinetic inductance detectors based on disordered films of granular aluminum [33] or nitride-based superconductors [34], for which the high normal state resistance of the metal film will provide a good power match to the radiation impedance of the antenna. It is quite possible that approaches to topologically protected qubits based on Majorana particles supported by superconducting-semiconducting heterostructures [35], for which quasiparticle poisoning is fatal [36], will be affected by the antenna coupling described here.

We extended our analysis to the case of radiation at the qubit frequency, for which the

qubit can be modeled as an electrically small antenna. Our modeling did not attempt to capture the impact of finite substrate thickness on the effective permittivity of the qubit medium, which will have a strong influence on radiative loss. However, even in the most optimistic scenario corresponding to $\epsilon_{\text{eff}} = 1$, we find a limit to qubit T_1 from radiation of order 1 ms. While the desire to protect against loss due to dielectric defects at interfaces motivates a push towards larger device scales [37], the need to limit radiative loss will provide an ultimate constraint on the size of qubit devices.

3.2 Experiments

We briefly describe an ongoing experiment attempting to test the model described in Chapter 2.

We mount a blackbody emitter above the superconducting thin film of a four-qubit chip and vary the temperature of the emitter from 80–500 mK¹. The extracted quasiparticle-induced upward transitions are shown in Figure 3.1 as a function of temperature, and indicate three distinct regimes for qubit radiation. The measurements discussed here correspond to Q4, as labeled in Figures 3.2 and 3.3 and Table 3.1, and are compared against a series of simulations of the exact qubits of this chip, which also suggest mutually compatible quasiparticle tunneling rates, as shown in Table 3.1 and Figure 3.3.

The resonance near 120 GHz, while of magnitude comparable to what we expect for resonant photon absorption, is roughly a factor of two smaller than the simulation results for Q4 shown in Figure 3.3. However, the simulations imply that this resonance corresponds to that of Q3; any resonant device with a Josephson junction may contribute to photon-assisted quasiparticle poisoning. Moreover, as shown in Figure 3.3, Q3 has a maximum coupling efficiency of greater magnitude than any other qubit. The spectral density of this radiation may further be amplified beyond that of Equation 2.7 by the resonant cavity the

¹Since the emitter subtends a significant solid angle of the qubit cavity and is significantly hotter than the chip itself, we approximate the effective temperature as the emitter temperature.

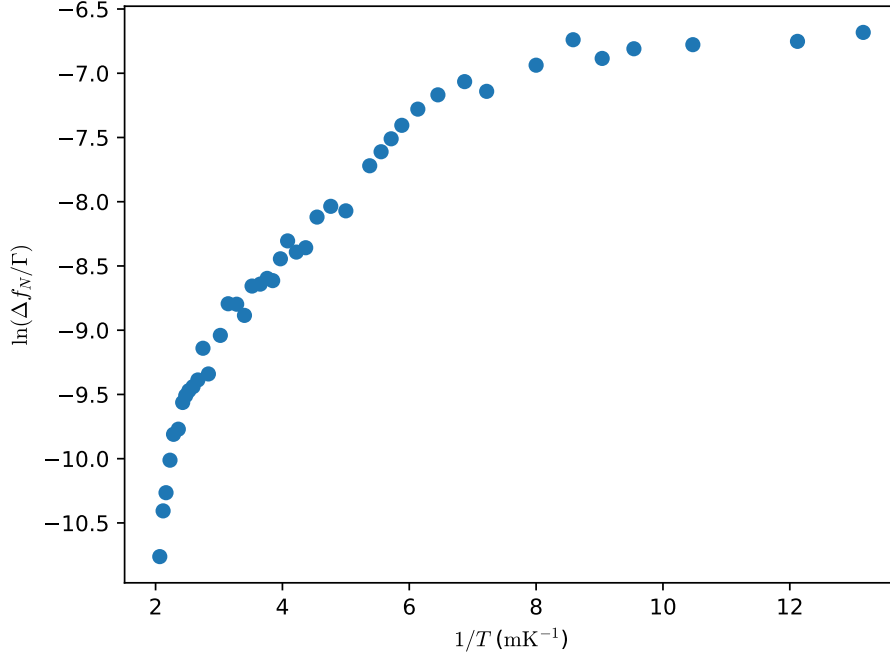


Figure 3.1: Upward QP-induced transitions vs temperature. The three visibly linear regions correspond to, with increasing temperature (right to left on the x axis), approximately 300 MHz, 10 GHz, and 120 GHz, respectively.

Qubit	r_o (μm)	r_i (μm)	Γ (Hz)	f_0 (GHz)
Q1	90	182	1042	244
Q2	50	52.9	19.7	370
Q3	108	500	282	128
Q4	70	90.5	79	242, 456

Table 3.1: Dependence of parity-switching on device scale, where qubits are shown schematically in Figure 3.2, and Γ is the associated quasiparticle tunneling rate [38]. Tunneling rate scales with device size, with the exception of Q3, where the gap between the qubit island and groundplane is several times larger than the island itself, and so does not conform particularly well to an antenna model. f_0 is the frequency of greatest coupling between the qubit structure, as simulated by a finite-element solver [26], and a junction of $C_j = 3$ fF and $R_n = 12.8$ k Ω .

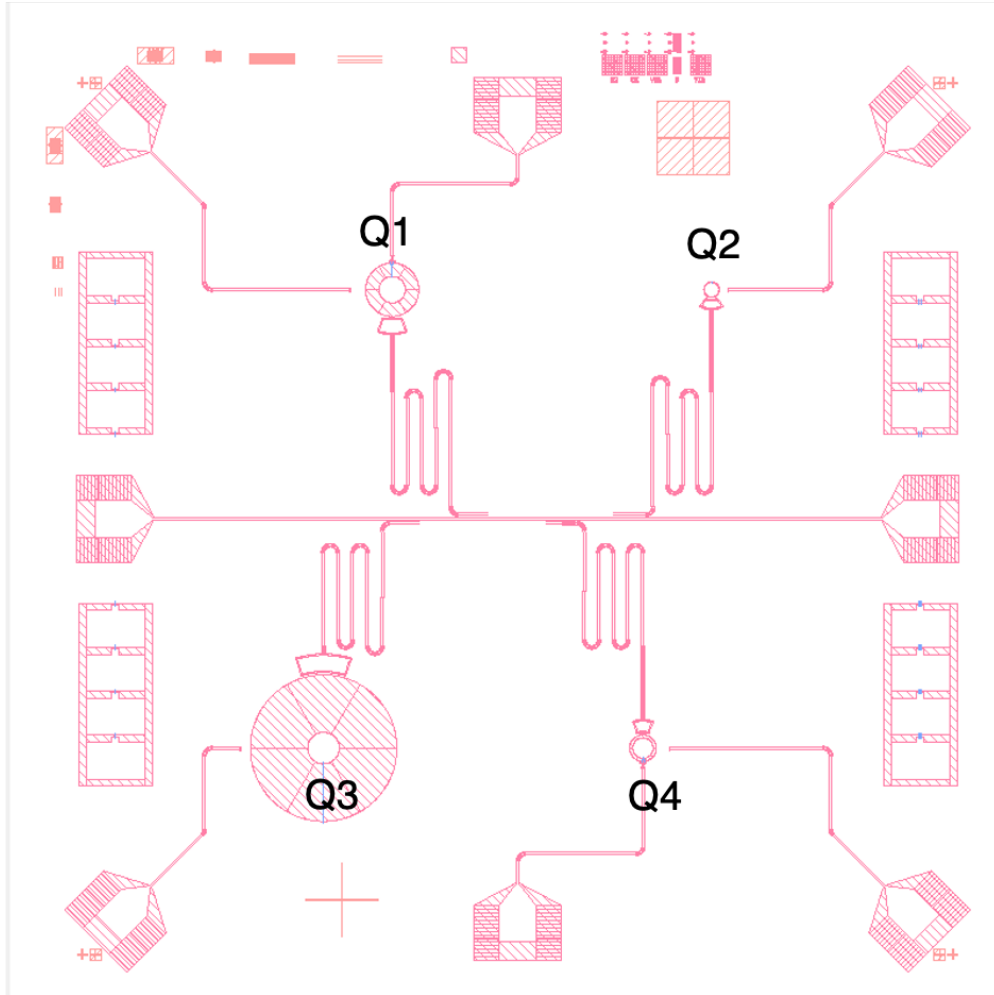


Figure 3.2: Weakly charge-sensitive transmons of various scales.

chip is housed in. We therefore expect that this device will dominate photon absorption.

At first blush, it appeared that the resonance near 10 GHz indicated that the qubit may be radiating at its own frequency. With higher resolution data, however, it became clear that this was not the case. This may instead be due to a spurious coupling between the qubit and other features of the chip—this frequency is compatible with a half-wave resonance of the coplanar-waveguide of length 5 mm bisecting the chip. If this is indeed the case, we expect a Purcell limit to this resonance and thus a de-Qing of the resonance with higher temperature. This is suggested by the data in Figure 3.1.

The source of the resonance at 300 MHz is not immediately clear. It is near that of the

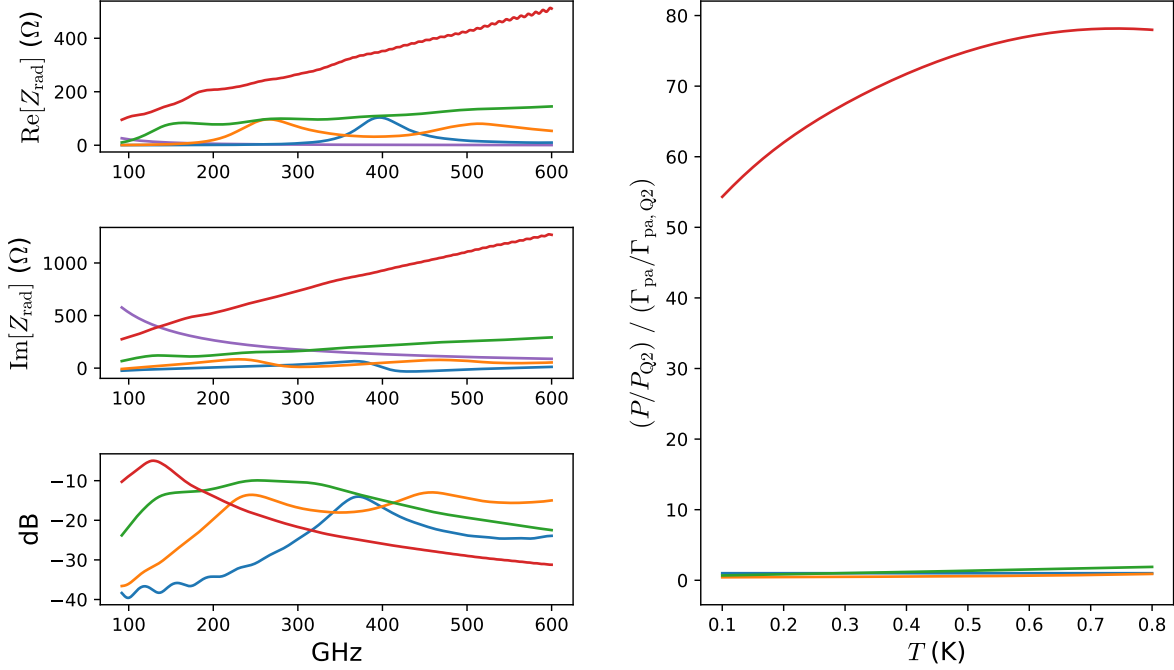


Figure 3.3: Device scale-dependent impedance simulations. Left: Real (top) and imaginary (middle) parts of qubit radiation impedance for Q1 (green), Q2 (blue), Q3 (red), and Q4 (orange). Conjugate junction impedance is shown in purple. The bottom plot shows coupling efficiencies for each of the four devices, with the color scheme as the top and middle plots. Right: Total coupled power over the range of the simulation normalized to measured tunneling rates from Table 3.1, each normalized to that of the smallest (and therefore most idealized) qubit, Q2. Q1, Q2, and Q4, appear mutually compatible with each other at various temperatures. The coupled power in Q3, however, is about a factor of 70 greater.

qubit anharmonicity, or the difference between the transition frequencies for the ground and first and first and second excited states, ω_{01} and ω_{12} , respectively, and so may indicate direct driving of both of these transitions and thus a beat frequency.

3.3 Applications

We briefly describe how the implications of resonant absorption described in Chapter 2 may be exploited for quantum sensing, specifically detection of dark matter axions.

A bad qubit, that is, one with strong coupling to its environment, is a good quantum

sensor. Superconducting devices are well-suited for, among other things, sensing in the far-infrared to microwave range, and have seen various uses therein over the past several decades [39–41]. Moreover, for the majority of the 20th century, practical technologies for generation and detection of radiation in this region of phase space have generally been restricted to niche applications in astronomy [42].

A detailed understanding of antenna coupling to pair-breaking photons will allow the engineering of optimized detectors of photons in the 10s of GHz to THz range for the purposes of, for example, narrowband spectroscopy of the cosmic microwave background or for detection of dark matter axions [43]. Antenna coupling to the radiation field will allow controlled transduction of photons to quasiparticles at the junction. These quasiparticles could be detected directly, or superconducting gap engineering [44] could be used to guide the generated quasiparticles to a separate qubit structure that would detect the change of quasiparticle parity with high fidelity [6, 29, 45].

Here, a “folded monopole” configuration is useful (Fig. 3.4), as the location of the junction at the edge of the antenna provides access to the quasiparticles generated across the array, and the aspect ratio allows integration of multiple antennas side-by-side.

Fabrication of such an array warrants several considerations. As detection of dark matter has proven to be an elusive feat due to characteristically weak interactions with forces other than gravity, the first and foremost consideration is to maximize sensing area at discrete frequencies. While this is straightforward for a single antenna, achieving a narrowband response in an array is, due to fabrication constraints, more difficult. For example, while varying aspect ratios and spacing across the array may yield a higher-Q resonance and provide some degree of filtering, engineering such an array is typically more difficult than keeping such parameters uniform [17]. On the other hand, given what little is known about the axion mass range and the distribution of particles therein, broadband absorption may prove more useful.

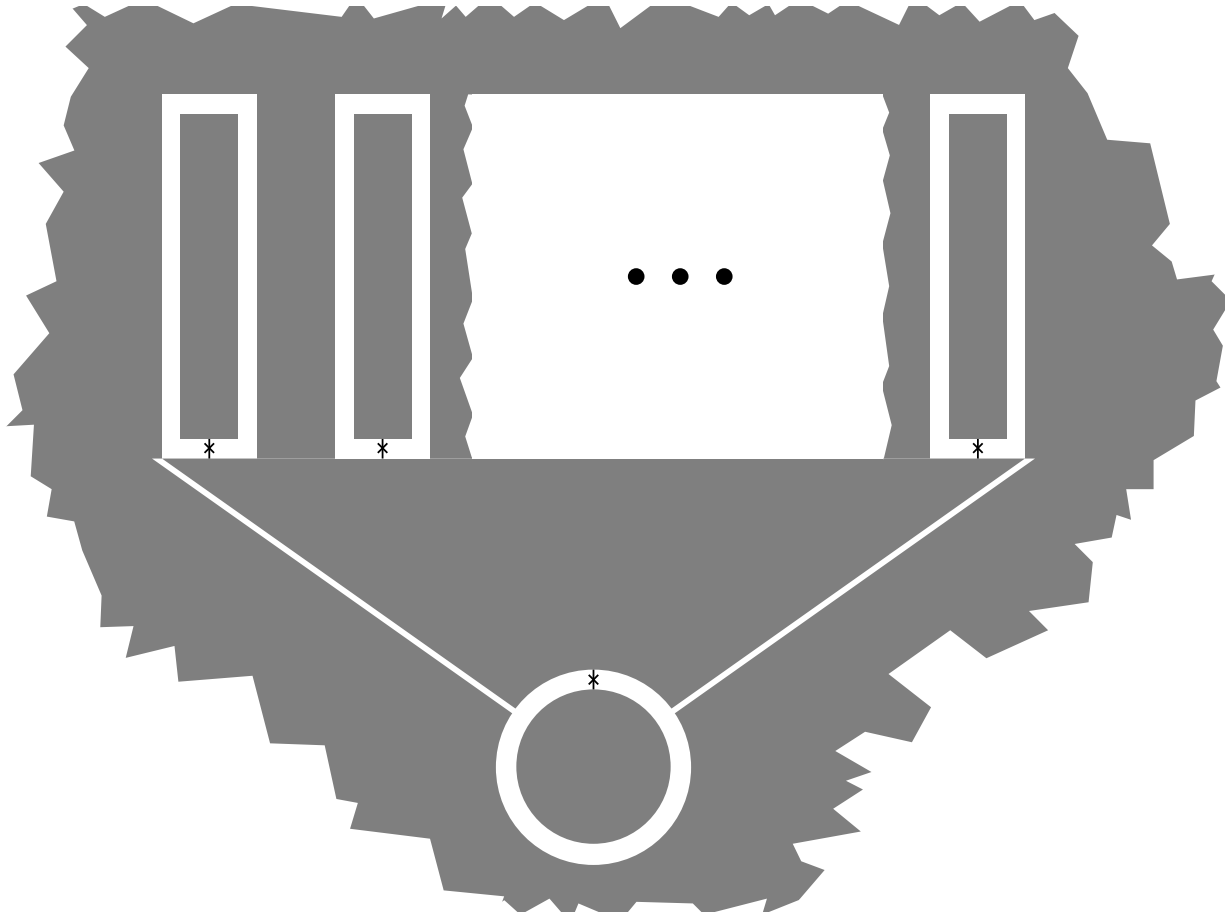


Figure 3.4: Folded monopole antenna array. Pair-breaking photons transduced from dark matter axions may be absorbed by any antenna in the array, generating a quasiparticle once coupled to the Josephson junction. The quasiparticles are then channeled to a single parity-sensing qubit. We do not expect quasiparticle recombination to be an issue considering the incredible weak signals expected from a dark matter detector.

DISCARD THIS PAGE

Colophon

This thesis was typeset with L^AT_EX and uses Gyre Pagella; it is based on a template by Will Benton located at

<https://github.com/willb/wi-thesis-template>.

Some modifications are based on the doctoral dissertation of Dr. Edward M. Leonard Jr., located at

<https://gitlab.com/eleonardjr/thesis>,

and the BibTeX citation style is a modified version of `apsrev4-2.bst`.

Computations were performed using Python via `numpy` [46], and plots were generated using `matplotlib` [47]. Vector graphics were (unfortunately) created using Microsoft PowerPoint.

Last update: 17 May 2021

Bibliography

- [1] O. Rafferty, S. Patel, C. H. Liu, S. Abdullah, C. D. Wilen, D. C. Harrison, and R. McDermott, *Spurious antenna modes of the transmon qubit*, [arXiv:2103.06803 \[quant-ph\]](https://arxiv.org/abs/2103.06803) (2021).
- [2] B. D. Josephson, *Possible new effects in superconductive tunnelling*, *Phys. Lett.* **1**, 251 (1962).
- [3] M. Kjaergaard, M. E. Schwartz, J. Braumüller, P. Krantz, J. I.-J. Wang, S. Gustavsson, and W. D. Oliver, *Superconducting qubits: Current state of play*, *Annu. Rev. Condens. Matter Phys.* **11**, 369 (2020).
- [4] J. M. Martinis, M. Ansmann, and J. Aumentado, *Energy decay in superconducting Josephson-junction qubits from nonequilibrium quasiparticle excitations*, *Phys. Rev. Lett.* **103**, 097002 (2009).
- [5] C. Wang, Y. Y. Gao, I. M. Pop, U. Vool, C. Axline, T. Brecht, R. W. Heeres, L. Frunzio, M. H. Devoret, G. Catelani, L. I. Glazman, and R. J. Schoelkopf, *Measurement and control of quasiparticle dynamics in a superconducting qubit*, *Nat. Commun.* **5**, 5836 (2014).
- [6] K. Serniak, M. Hays, G. de Lange, S. Diamond, S. Shankar, L. D. Burkhardt, L. Frunzio, M. Houzet, and M. H. Devoret, *Hot nonequilibrium quasiparticles in transmon qubits*, *Phys. Rev. Lett.* **121**, 157701 (2018).
- [7] K. Serniak, S. Diamond, M. Hays, V. Fatemi, S. Shankar, L. Frunzio, R. J. Schoelkopf, and M. H. Devoret, *Direct dispersive monitoring of charge parity in offset-charge-sensitive transmons*, *Phys. Rev. Applied* **12**, 014052 (2019).
- [8] G. Catelani, J. Koch, L. Frunzio, R. J. Schoelkopf, M. H. Devoret, and L. I. Glazman, *Quasiparticle relaxation of superconducting qubits in the presence of flux*, *Phys. Rev. Lett.* **106**, 077002 (2011).
- [9] A. P. Vepsäläinen, A. H. Karamlou, J. L. Orrell, A. S. Dogra, B. Loer, F. Vasconcelos, D. K. Kim, A. J. Melville, B. M. Niedzielski, J. L. Yoder, S. Gustavsson, J. A. Formaggio, B. A. VanDevender, and W. D. Oliver, *Impact of ionizing radiation on superconducting qubit coherence*, *Nature* **584**, 551 (2020).
- [10] C. D. Wilen, S. Abdullah, N. A. Kurinsky, C. Stanford, L. Cardani, G. D’Imperio, C. Tomei, L. Faoro, L. B. Ioffe, C. H. Liu, A. Opremcak, B. G. Christensen, J. L. DuBois,

- and R. McDermott, *Correlated charge noise and relaxation errors in superconducting qubits*, arXiv:2012.06029 [quant-ph] (2020).
- [11] U. Patel, I. V. Pechenezhskiy, B. L. T. Plourde, M. G. Vavilov, and R. McDermott, *Phonon-mediated quasiparticle poisoning of superconducting microwave resonators*, *Phys. Rev. B* **96**, 220501(R) (2017).
- [12] M. Houzet, K. Serniak, G. Catelani, M. H. Devoret, and L. I. Glazman, *Photon-assisted charge-parity jumps in a superconducting qubit*, *Phys. Rev. Lett.* **123**, 107704 (2019).
- [13] R. Barends, J. Wenner, M. Lenander, Y. Chen, R. C. Bialczak, J. Kelly, E. Lucero, P. O'Malley, M. Mariantoni, D. Sank, H. Wang, T. C. White, Y. Yin, J. Zhao, A. N. Cleland, J. M. Martinis, and J. J. A. Baselmans, *Minimizing quasiparticle generation from stray infrared light in superconducting quantum circuits*, *Appl. Phys. Lett.* **99**, 113507 (2011).
- [14] A. D. Córcoles, J. M. Chow, J. M. Gambetta, C. Rigetti, J. R. Rozen, G. A. Keefe, M. B. Rothwell, M. B. Ketchen, and M. Steffen, *Protecting superconducting qubits from radiation*, *Appl. Phys. Lett.* **99**, 181906 (2011).
- [15] J. Koch, T. M. Yu, J. Gambetta, A. A. Houck, D. I. Schuster, J. Majer, A. Blais, M. H. Devoret, S. M. Girvin, and R. J. Schoelkopf, *Charge-insensitive qubit design derived from the Cooper pair box*, *Phys. Rev. A* **76**, 042319 (2007).
- [16] A. A. Houck, J. A. Schreier, B. R. Johnson, J. M. Chow, J. Koch, J. M. Gambetta, D. I. Schuster, L. Frunzio, M. H. Devoret, S. M. Girvin, and R. J. Schoelkopf, *Controlling the spontaneous emission of a superconducting transmon qubit*, *Phys. Rev. Lett.* **101**, 080502 (2008).
- [17] C. A. Balanis, *Antenna Theory: Analysis and Design*, 4th ed. (Wiley, 2016).
- [18] R. Barends, J. Kelly, A. Megrant, D. Sank, E. Jeffrey, Y. Chen, Y. Yin, B. Chiaro, J. Mutus, C. Neill, P. O'Malley, P. Roushan, J. Wenner, T. C. White, A. N. Cleland, and J. M. Martinis, *Coherent Josephson qubit suitable for scalable quantum integrated circuits*, *Phys. Rev. Lett.* **111**, 080502 (2013).
- [19] J. M. Chow, J. M. Gambetta, A. D. Córcoles, S. T. Merkel, J. A. Smolin, C. Rigetti, S. Poletto, G. A. Keefe, M. B. Rothwell, J. R. Rozen, M. B. Ketchen, and M. Steffen, *Universal quantum gate set approaching fault-tolerant thresholds with superconducting qubits*, *Phys. Rev. Lett.* **109**, 060501 (2012).
- [20] A. P. M. Place, L. V. H. Rodgers, P. Mundada, B. M. Smitham, M. Fitzpatrick, Z. Leng, A. Premkumar, J. Bryon, A. Vrajitoarea, S. Sussman, G. Cheng, T. Madhavan, H. K. Babla, X. H. Le, Y. Gang, B. Jäck, A. Gyenis, N. Yao, R. J. Cava, N. P. de Leon, and A. A. Houck, *New material platform for superconducting transmon qubits with coherence times exceeding 0.3 milliseconds*, *Nat. Commun.* **12**, 1779 (2021).

- [21] H. Paik, D. I. Schuster, L. S. Bishop, G. Kirchmair, G. Catelani, A. P. Sears, B. R. Johnson, M. J. Reagor, L. Frunzio, L. I. Glazman, S. M. Girvin, M. H. Devoret, and R. J. Schoelkopf, *Observation of high coherence in Josephson junction qubits measured in a three-dimensional circuit QED architecture*, *Phys. Rev. Lett.* **107**, 240501 (2011).
- [22] A. G. Fowler, M. Mariantoni, J. M. Martinis, and A. N. Cleland, *Surface codes: Towards practical large-scale quantum computation*, *Phys. Rev. A* **86**, 032324 (2012).
- [23] J. Preskill, *Quantum computing in the NISQ era and beyond*, *Quantum* **2**, 79 (2018).
- [24] F. Arute, K. Arya, R. Babbush, D. Bacon, J. C. Bardin, R. Barends, R. Biswas, S. Boixo, F. G. S. L. Brandao, D. A. Buell, B. Burkett, Y. Chen, Z. Chen, B. Chiaro, R. Collins, W. Courtney, A. Dunsworth, E. Farhi, B. Foxen, A. Fowler, C. Gidney, M. Giustina, R. Graff, K. Guerin, S. Habegger, M. P. Harrigan, M. J. Hartmann, A. Ho, M. Hoffmann, T. Huang, T. S. Humble, S. V. Isakov, E. Jeffrey, Z. Jiang, D. Kafri, K. Kechedzhi, J. Kelly, P. V. Klimov, S. Knysh, A. Korotkov, F. Kostritsa, D. Landhuis, M. Lindmark, E. Lucero, D. Lyakh, S. Mandrà, J. R. McClean, M. McEwen, A. Megrant, X. Mi, K. Michielsen, M. Mohseni, J. Mutus, O. Naaman, M. Neeley, C. Neill, M. Y. Niu, E. Ostby, A. Petukhov, J. C. Platt, C. Quintana, E. G. Rieffel, P. Roushan, N. C. Rubin, D. Sank, K. J. Satzinger, V. Smelyanskiy, K. J. Sung, M. D. Trevithick, A. Vainsencher, B. Villalonga, T. White, Z. J. Yao, P. Yeh, A. Zalcman, H. Neven, and J. M. Martinis, *Quantum supremacy using a programmable superconducting processor*, *Nature* **574**, 505 (2019).
- [25] F. S. Henyey, *Distinction between a perfect conductor and a superconductor*, *Phys. Rev. Lett.* **49**, 416 (1982).
- [26] CST Studio Suite, <https://cst.com> (2021).
- [27] V. Ambegaokar and A. Baratoff, *Tunneling between superconductors*, *Phys. Rev. Lett.* **10**, 486 (1963).
- [28] M. Steffen, F. Brito, D. DiVincenzo, S. Kumar, and M. Ketchen, *Decoherence of floating qubits due to capacitive coupling*, *New J. Phys.* **11**, 033030 (2009).
- [29] B. G. Christensen, C. D. Wilen, A. Opremcak, J. Nelson, F. Schlenker, C. H. Zimonick, L. Faoro, L. B. Ioffe, Y. J. Rosen, J. L. DuBois, B. L. T. Plourde, and R. McDermott, *Anomalous charge noise in superconducting qubits*, *Phys. Rev. B* **100**, 140503(R) (2019).
- [30] S. Sendelbach, D. Hover, A. Kittel, M. Mück, J. M. Martinis, and R. McDermott, *Calculations for magnetism in squids at millikelvin temperatures*, arXiv:0802.1511 [cond-mat.supr-con] (2008).
- [31] V. E. Manucharyan, J. Koch, L. I. Glazman, and M. H. Devoret, *Fluxonium: Single Cooper-pair circuit free of charge offsets*, *Science* **326**, 113 (2009).
- [32] F. Yan, S. Gustavsson, A. Kamal, J. Birenbaum, A. P. Sears, D. Hover, T. J. Gudmundsen, D. Rosenberg, G. Samach, S. Weber, J. L. Yoder, T. P. Orlando, J. Clarke, A. J. Kerman, and W. D. Oliver, *The flux qubit revisited to enhance coherence and reproducibility*, *Nat. Commun.* **7**, 12964 (2016).

- [33] F. Henriques, F. Valenti, T. Charpentier, M. Lagoin, C. Gouriou, M. Martínez, L. Cardani, M. Vignati, L. Grünhaupt, D. Gusenkova, J. Ferrero, S. T. Skacel, W. Wernsdorfer, A. V. Ustinov, G. Catelani, O. Sander, and I. M. Pop, *Phonon traps reduce the quasiparticle density in superconducting circuits*, *Appl. Phys. Lett.* **115**, 212601 (2019).
- [34] R. Barends, N. Verduyn, A. Endo, P. J. de Visser, T. Zijlstra, T. M. Klapwijk, and J. J. A. Baselmans, *Reduced frequency noise in superconducting resonators*, *Appl. Phys. Lett.* **97**, 033507 (2010).
- [35] R. M. Lutchyn, J. D. Sau, and S. Das Sarma, *Majorana fermions and a topological phase transition in semiconductor-superconductor heterostructures*, *Phys. Rev. Lett.* **105**, 077001 (2010).
- [36] D. Rainis and D. Loss, *Majorana qubit decoherence by quasiparticle poisoning*, *Phys. Rev. B* **85**, 174533 (2012).
- [37] J. M. Martinis, K. B. Cooper, R. McDermott, M. Steffen, M. Ansmann, K. D. Osborn, K. Cicak, S. Oh, D. P. Pappas, R. W. Simmonds, and C. C. Yu, *Decoherence in Josephson qubits from dielectric loss*, *Phys. Rev. Lett.* **95**, 210503 (2005).
- [38] C. D. Wilen, private communication (2021).
- [39] J. Clarke, G. I. Hoffer, P. L. Richards, and N. H. Yeh, *Superconductive bolometers for submillimeter wavelengths*, *J. Appl. Phys.* **48**, 4865 (1977).
- [40] P. M. Echternach, B. J. Pepper, T. Reck, and C. M. Bradford, *Single photon detection of 1.5 THz radiation with the quantum capacitance detector*, *Nat. Astron.* **2**, 90 (2017).
- [41] A. V. Dixit, S. Chakram, K. He, A. Agrawal, R. K. Naik, D. I. Schuster, and A. Chou, *Searching for dark matter with a superconducting qubit*, *Phys. Rev. Lett.* **126**, 141302 (2021).
- [42] S. S. Dhillon, M. S. Vitiello, E. H. Linfield, A. G. Davies, M. C. Hoffmann, J. Booske, C. Paoloni, M. Gensch, P. Weightman, G. P. Williams, E. Castro-Camus, D. R. S. Cumming, F. Simoens, I. Escorcia-Carranza, J. Grant, S. Lucyszyn, M. Kuwata-Gonokami, K. Konishi, M. Koch, C. A. Schmuttenmaer, T. L. Cocker, R. Huber, A. G. Markelz, Z. D. Taylor, V. P. Wallace, J. A. Zeitler, J. Sibik, T. M. Korter, B. Ellison, S. Rea, P. Goldsmith, K. B. Cooper, R. Appleby, D. Pardo, P. G. Huggard, V. Krozer, H. Shams, M. Fice, C. Renaud, A. Seeds, A. Stöhr, M. Naftaly, N. Ridler, R. Clarke, J. E. Cunningham, and M. B. Johnston, *The 2017 terahertz science and technology roadmap*, *J. Phys. D: Appl. Phys.* **50**, 043001 (2017).
- [43] T. Braine, R. Cervantes, N. Crisosto, N. Du, S. Kimes, L. J. Rosenberg, G. Rybka, J. Yang, D. Bowring, A. S. Chou, R. Khatiwada, A. Sonnenschein, W. Wester, G. Carosi, N. Woollett, L. D. Duffy, R. Bradley, C. Boutan, M. Jones, B. H. LaRoque, N. S. Oblath, M. S. Taubman, J. Clarke, A. Dove, A. Eddins, S. R. O'Kelley, S. Nawaz, I. Siddiqi, N. Stevenson, A. Agrawal, A. V. Dixit, J. R. Gleason, S. Jois, P. Sikivie, J. A. Solomon, N. S. Sullivan, D. B. Tanner, E. Lentz, E. J. Daw, J. H. Buckley, P. M. Harrington, E. A. Henriksen, and K. W. Murch (ADMX Collaboration), *Extended search for the invisible axion with the axion dark matter experiment*, *Phys. Rev. Lett.* **124**, 101303 (2020).

- [44] J. Aumentado, M. W. Keller, J. M. Martinis, and M. H. Devoret, *Nonequilibrium quasiparticles and $2e$ periodicity in single-Cooper-pair transistors*, *Phys. Rev. Lett.* **92**, 066802 (2004).
- [45] D. Ristè, C. C. Bultink, M. J. Tiggelman, R. N. Schouten, K. W. Lehnert, and L. DiCarlo, *Millisecond charge-parity fluctuations and induced decoherence in a superconducting transmon qubit*, *Nat. Commun.* **4**, 1913 (2013).
- [46] C. R. Harris, K. J. Millman, S. J. van der Walt, R. Gommers, P. Virtanen, D. Cournapeau, E. Wieser, J. Taylor, S. Berg, N. J. Smith, R. Kern, M. Picus, S. Hoyer, M. H. van Kerkwijk, M. Brett, A. Haldane, J. F. del Río, M. Wiebe, P. Peterson, P. Gérard-Marchant, K. Sheppard, T. Reddy, W. Weckesser, H. Abbasi, C. Gohlke, and T. E. Oliphant, *Array programming with NumPy*, *Nature* **585**, 357 (2020).
- [47] J. D. Hunter, *Matplotlib: A 2D graphics environment*, *Comput. Sci. Eng.* **9**, 90 (2007).